Enhanced electrical and photocatalytic activities in $Na_{0.5}Bi_{0.5}TiO_3$ through structural modulation by using anatase and rutile phases of TiO_2

Cilaveni Goutham [a], Kinjarapu Venkata Ashok Kumar [b], Sai Santosh Kumar Raavi [a], Challapalli Subrahmanyam [b], Saket Asthana [a, *]

[a] Advanced Functional Materials Laboratory, Department of Physics, Indian Institute of Technology Hyderabad, Kandi, Sangareddy, 502285, Telangana, India
[b] Department of Chemistry, Indian Institute of Technology Hyderabad, Kandi, Sangareddy, 502285, Telangana, India

ABSTRACT

This paper deals with an in-depth analysis on the role of the microstructure phase of titanium dioxide (TiO_2) precursor in sodium bismuth titanate ($Na_{0.5}Bi_{0.5}TiO_3$, hereafter represented as NBT) ceramics prepared through the hydrothermal method. The comparison of the grain size, microstructure, crystal structure, and electrical properties of the NBT ceramics is carried out using anatase and rutile TiO_2. NBT ceramics with anatase TiO_2 (denoted by NBT_A) displayed superior dielectric and ferro/piezoelectric properties along with the additional functionality in terms of photocatalysis. Systematic studies of functional properties such as piezoelectric, ferroelectric, and dielectric stressed the far-reaching influence of effects on grain size. The mechanisms and functional properties of grain quantitative effects are also discussed. Grain boundaries volume fraction increment has decreased the dielectric peak but increased the diffusiveness in the case of the NBT with rutile TiO_2 precursor (denoted as NBT_R). Similarly, elastic stiffness increment restricts the movement of the domain wall and led to a decrement in remnant polarization along with an increase in the values of the corresponding piezoelectric coefficient in fine-grain NBT_R samples.

1. Introduction

Miniaturization and nanoengineering of electronic devices have advanced investigations into the synthesis of many nanostructured materials. It is crucial and challenging to use the micro/nanoscale piezoelectric materials with controlled morphology in applications such as advanced sensors, actuators, transducers, storage devices, *etc.* [1,2]. In the last few decades, the piezo-ceramics, which dominated this field of application, are Pb-based systems such as $PbZrO_3$-$PbTiO_3$ (PZT), $Pb(Mg_{1/2}Nb_{3/2})O_3$-$PbTiO_3$ (PMN-PT), $BiScO_3$-$PbTiO_3$ (BS-PT), *etc.*, [3,4]. The application potentiality of these lead-based systems is mainly derived from their high ferroelectric Curie temperature (T_c) and their large electromechanical response with a high piezo coefficient (d_{33}) around 300–500 pC/N. Research into environmentally friendly piezoelectric materials has increased in recent years, primarily for ecological and health concerns. Recently, innumerable lead-free compounds such as $Na_{0.5}Bi_{0.5}TiO_3$ (NBT), $BaTiO_3$ (BTO), $K_{0.5}Na_{0.5}NbO_3$ (KNN), $K_{0.5}Bi_{0.5}TiO_3$ (KBT), and their binary and ternary solid solutions with competent electrical properties are extensively investigated [5–8].

Sodium Bismuth Titanate (NBT), a well-known electro ceramic, has a perovskite structure at ambient temperatures. NBT is one of the few ferroelectric materials that play a pioneering role in lead-free ferroelectric materials and is a viable alternative to lead-based piezoceramics materials. This ferroelectric material has gained enormous recognition in the solid-state process in recent decades because of outstanding dielectric and ferroelectric properties with high Curie temperature ($T_c = 320\,°C$) and large remnant polarization ($P_r = 38\ \mu C/cm^2$) [9–12]. However, high electrical conductivity in the material makes the poling process difficult. A low-temperature synthesis route can be adopted along with densifying grains that are randomly oriented which are necessary to control the charge carrier percolation channels, to overcome this difficulty.

In general, characteristic properties such as d_{33}, remnant polarization (P_r), and coercive field (E_c) of piezoelectric and ferroelectric materials are greatly affected by various factors such as density, grain size, *etc.*, which are controlled by the synthesis conditions and precursors used [13]. Although the effects of different synthesis conditions on the phase formation adopted for NBT are described thoroughly [14], the selection of different structural phase precursors to be used for the preparation and the effects on the electrical properties are not to our understanding. Titanium dioxide (TiO$_2$) exists in three forms in nature namely brookite, rutile, and anatase. The TiO$_2$ with anatase and rutile structure contains titanium with six-coordination in a stable form as compared to that of brookite-type TiO$_2$ [15,16]. Therefore, the use of TiO$_2$ is described in detail without much insight into its effects on the ferro/piezoelectric properties.

NBT ceramics are commonly synthesized through the solid-state method, giving grains of micrometer size that are mechanically unstable and restrict their implementation feasibility in miniaturized devices. The preparation of non-agglomerated particles in the micrometer and nano-size provides feasibility in using them as building blocks for electronic components. Micron and nano-sized NBT crystals are previously prepared using the hydrothermal method, sol-gel technique, *etc.*, [17]. In contrast to many high-temperature techniques, hydrothermal synthesis is regarded as the ideal process for cost-effective ceramic powder production at lower temperatures with exact stoichiometry, homogeneity, and uniform size distribution. The role of various parameters (temperature, time, pH, precursors) involved during the hydrothermal synthesis and also the Bi/Ti ratio was investigated recently [18–21]. The hydrothermal production of NBT nanostructures such as nanorods, nanowires, and nanocubes has already been described by several authors in the literature [22–24]. Improvement in the surface-to-volume ratio and reduction in the crystal defects are obtained in nanocubes. Uniformly designed micro-and nano cubic crystals are focussed extensively due to their distinctive properties and also in their role as building blocks for electronic components. Li *et al.* [25] prepared cubic NBT powders with sizes of particles in the range of 3.5–5.5 μm by a hydrothermal process with a varied range of NaOH concentration from 2 to 12 mol/L. Accordingly, NBT powders with single-phase were produced from TiO$_2$ and Bi(NO$_3$)$_3$·5H$_2$O precursors under a strongly alkaline environment at 200 °C. By controlling the size and shape of the NBT particles, it is believed that the electronic and surface structures promote the photocatalyst activity. The cubic nanoparticles surface structure has surfaces with a precisely defined arrangement of atoms. This will influence the photocatalytic properties both in terms of selectivity and activity. Therefore, cubic NBT powders were extensively studied because of their high surface-to-volume ratio, which can be also used in various potential and interdisciplinary applications such as photocatalysis as briefly explained in the following section.

The removal of harmful chemicals present in wastewater has recently become more important. According to the reports, the wastewater from the textile industry contains dyes that are detrimental to the aquatic environment [26–28]. This has triggered the removal of harmful chemicals present in the wastewater and numerous physical and chemical remedial measures like ion exchange, membrane filtration, and activated carbon adsorption have been developed while these processes have disadvantages in producing concentrated sludge production and/or secondary pollutants, low efficiency, and high cost [29,30]. Because of its lower toxicity, and higher dye degradation efficiency of the macromolecules, photocatalysis has been studied. In particular, much attention has been paid to photocatalysts that are oxide semiconductors, for
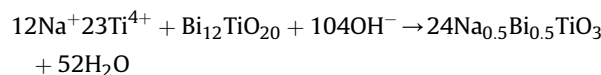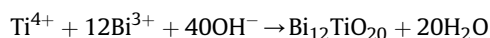
the degradation of the organic chemicals from sewerage by a photocatalysis-based advanced oxidation process (AOP). The macron-scaled dye molecules are either mineralized or converted into less harmful and smaller molecules triggered by OH radicals i.e., strongly oxidizing agents through a series of oxidation processes. Among the oxides, perovskite oxides exhibit photostability and excellent photocatalytic activity due to major lattice distortion and defects that help trap holes and inhibit the electron-hole pair's recombination rate [31]. The oxygen absorption at the surface cation sites is promoted by the metal cation and O^{2-} anion vacancies, which stimulate the photocatalytic reaction [32,33].

According to the discussion mentioned above, the study aims to investigate the mechanism of NBT formation, which is prepared through hydrothermal synthesis using a TiO$_2$ precursor with different phase structures as starting materials. The influence of different phase structures of TiO$_2$ on the structural and electrical properties of NBT was investigated. Besides, the photocatalytic activity of the NBT prepared in the decomposition of crystal violet (CV), methylene blue (MB), Rhodamine B (RhB) was investigated and correlated.

2. Experimental section

2.1. Sample preparation

The hydrothermal synthesis method was used to make Na$_{0.5}$Bi$_{0.5}$TiO$_3$ ceramics with anatase- and rutile- TiO$_2$ (represented as NBT$_A$ and NBT$_R$). Analytical reagent grade bismuth (III) nitrate pentahydrate (Bi(NO$_3$)$_3$·5H$_2$O) (Alfa Aesar Chemicals, USA, 98%) and titanium (IV) oxide (TiO$_2$) with anatase (Sigma Aldrich Chemicals, USA, 99.99%) and rutile (Alfa Aesar Chemicals, USA, 99.9%) phase structure powders were taken as starting precursors of bismuth and titanium and Sodium hydroxide (NaOH) was taken as a source of sodium cations while ensuring a highly alkaline ambiance. The bismuth to titanium ion ratio of 0.5 has been used, except in cases where it is expressed separately. The concentration of the precursor was given in terms of bismuth ions. The precursors of titanium and bismuth were mixed with 60 mL of deionized water. This was followed by the addition of NaOH solution having a concentration of 14 mol/L. A homogeneous solution was obtained by stirring for about half an hour using a magnetic stirrer. The solution was transferred into Teflon-lined stainless steel autoclaves with 60% filling capacity and held for 48 h at 200 °C under automatically generated pressure. After heating for the desired time, the autoclave with the solution was naturally cooled and the final products were obtained by washing using distilled water (pH of the solution was neutral) and dried in an oven at 80 °C to obtain NBT cubic crystals. The as-synthesized powders were ground and after adding 6% by weight of PVA as the binder, pressed uniaxially to form 8 mm cylindrical pellets. The resultant pellets were sintered at 1150 °C with a dwelling time of 3 h in air with an intermittent dwell time of ½ h at 600 °C to evaporate the binder. The samples synthesized with anatase- and rutile-type TiO$_2$ as precursors are hereafter called NBT$_A$ and NBT$_R$, respectively. A flow diagram of the hydrothermal synthesis followed is shown in Fig. 1. The formulation for the hydrothermal reaction of the present study is as follows:
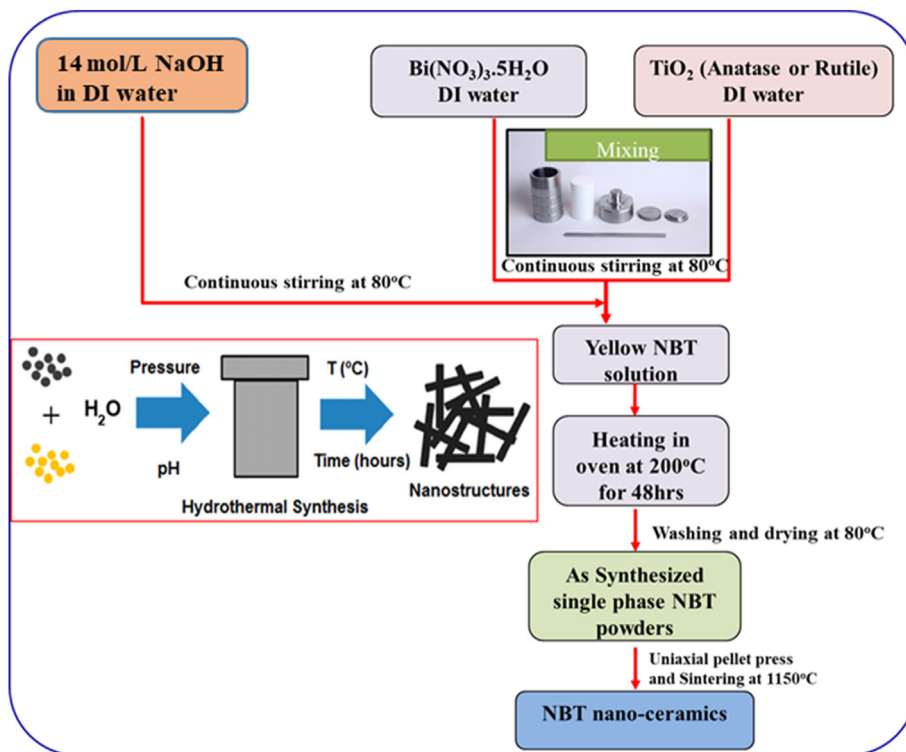
$$Ti^{4+} + 12Bi^{3+} + 40OH^- \rightarrow Bi_{12}TiO_{20} + 20H_2O$$

$$12Na^+ 23Ti^{4+} + Bi_{12}TiO_{20} + 104OH^- \rightarrow 24Na_{0.5}Bi_{0.5}TiO_3 + 52H_2O$$

Fig. 1. Flow chart of a hydrothermal method for synthesizing NBT nano-ceramics.

2.2. Characterization methodology

The sintered ceramics were made into fine powders. These powders were annealed in closed crucibles for 4 h at 500 °C to relieve the residual stresses induced during milling. The polycrystalline powders crystallinity was examined by using X-ray diffraction (Rigaku Pro; CuK$_\alpha$ radiation $\lambda = 1.5406$ Å) at ambiance temperature over a Bragg angle of $20° \leq 2\theta \leq 80°$. Fullprof refinement software package was used for the Rietveld analysis of the X-ray diffraction data to acquire crystallographic information such as lattice parameters, and crystal structure [34]. The surface microstructure studies of the ceramics were carried out using energy-dispersive X-ray spectroscopy equipped Field emission scanning electron microscope (FESEM, Carl Zeiss, Supra 40) on the as-sintered surface of the sample. The distribution of mean grain size was approximated by analyzing the area information (*i.e.*, equivalent diameter) followed by statistical calculations over the entire FESEM image, carried out using ImageJ microscope software [35]. Energy-dispersive X-ray spectroscopy was used for the mapping of the elemental distribution. Theoretical (crystallographic) density and Archimedes principle were used to calculate the relative density. Circular surfaces on both sides of the sintered ceramics were polished and sputtered with silver to serve as electrodes for various electrical measurements. The complex nature of the dielectric permittivity was calculated using an alpha dielectric analyzer (Novocontrol) as a function of frequency from 10 Hz to 1000 kHz and temperature from 40 to 500 °C. The polarization (P) and the strain measurements with the electric field (E) were carried out on samples with a thickness of 0.6 mm using a TF-Analyzer 2000 (aixACCT systems, GmbH). Using the combination of a high voltage amplifier and a function generator, sine waves of low-frequency (1 Hz) and high voltage were applied whereas a charge-to-voltage converter is used to measure the charge.

The surface area of NBT$_A$ and NBT$_R$ samples was measured using a NOVA 2200e BET analyzer (Quantachrome instruments). The nitrogen adsorption and desorption isotherm at -196.15 °C was also measured after the sample was dried at 100 °C. The photocatalytic activity of NBT catalyst prepared in this way was examined by bleaching solvated dye in the aqueous solutions of dyes Rhodamine B (RhB), crystal violet (CV), and methylene blue (MB). The as-synthesized NBT catalysts were tested in a specially developed photoreactor, that is operated by halogen-free lamps (24 V) with 250 W, which emits a visible light intensity of 750−800 Wm^{-2}. The starting concentration of the solution with dye was 50 mg/L. The ceramic powders together with the catalysts kept in the reactor and left in dark conditions with stirring for 30 min to attain an absorption-desorption equilibrium. After 30 min of exposure, the dye solution was collected in small aliquots (1−2 mL) and centrifuged (2000 rpm). The efficiency of the degradation process was assessed by monitoring the dye decolorization with respect to exposure time using a UV−Vis spectrophotometer. The efficiency of the photocatalytic dye degradation was measured using

$$\eta = (C_o - C)/_{C_o} \times 100\%$$

where the starting concentration is C_o, the concentration after time t is C, and the efficiency of the photocatalytic dye degradation is given by η.

3. Results and discussion

3.1. Influence of TiO$_2$ structure variants on the NBT structure

Fig. 2 shows the two stable phase structures of TiO$_2$. Anatase structure (A, PDF#89−4921) in Fig. 2(a) and a rutile structure (R, PDF#21−1276) in Fig. 2(b). The diffracted peaks agree with the indicated tetragonal phase. However, the formation of TiO$_2$ of the rutile-type from TiO$_2$ of the anatase-type takes place at a
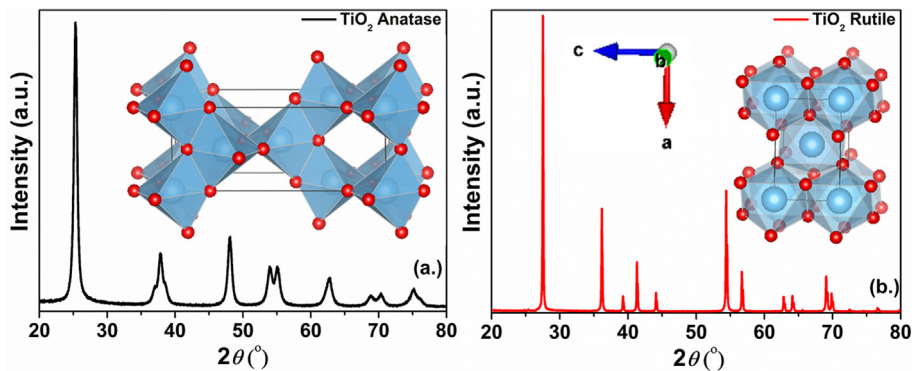
C. Goutham, K.V. Ashok Kumar, S.S. Kumar Raavi et al.

Fig. 2. X-ray diffraction patterns of (a) anatase TiO_2 and (b) rutile TiO_2 structure (inset shows the 3D polyhedral model of the specified phase).
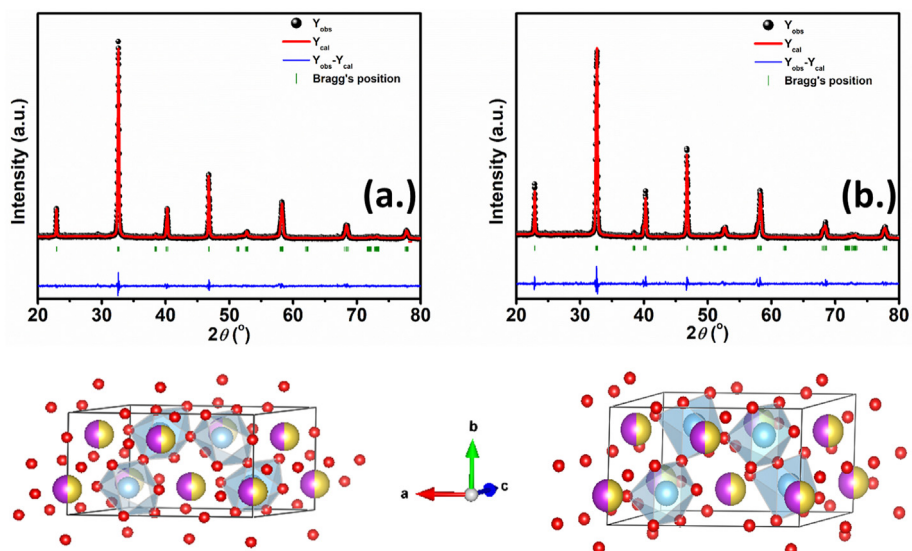

Fig. 3. Rietveld graphical output of (a) NBT_A and (b) NBT_R ceramics along with the monoclinic Cc phase drawn using VESTA package. The reflections position corresponding to the monoclinic phase is indicated by vertical bars.

calcination temperature of ~915 °C. The white NBT powders found in the autoclave after the synthesis were used to prepare pellets which are sintered at 1150 °C for 3 h. Fig. 3(a) and (b) represents the XRD pattern of the powdered samples of NBT_A and NBT_R ceramics obtained at ambiance temperature. The XRD patterns illustrate a pure perovskite structure with monoclinic space group Cc. No evidence of TiO_2 or Bi-related phases were detected in the XRD pattern, which indicates the formation of high-purity NBT ceramics within the XRD detection limit. In the NBT perovskite structure, each Na (Bi) atom is surrounded by twelve atoms of oxygen and forms $[NaO_{12}]$ clusters. Six oxygen atoms are bound to Ti atoms and form polar $[TiO_6]$ clusters. Ti atoms in the $[TiO_6]$ clusters are shifted slightly along the [001] direction which results from the covalent nature between the O-Ti-O bonds.

The single-phase monoclinic structure is confirmed by Rietveld refinement and shown in Fig. 3(a) and (b). A fullprof refinement software was used for the detailed profile analysis. Background correction was performed using linear interpolation and the pseudo-Voigt peak asymmetry function was used for fitting the XRD diffraction peak profiles. A 3D polyhedron model was generated depending on the last refined monoclinic phase profile using the VESTA software [36] and is shown below the respective representations of Fig. 3(a) and (b). The NBT phase structure has been controversial since its inception because it is often subtle and

Table 1
Refined structural parameters for NBT_A and NBT_R from Rietveld refinement.

Parameters	NBT_A	NBT_R
Lattice parameters (A°)	a = 9.5301(10)	a = 9.5514(7)
	b = 5.4762(4)	b = 5.4760(5)
	c = 5.5105(5)	c = 5.5152(6)
	β = 125.467(5)	β = 125.596(5)
Cell volume (A°)³	V = 234.22	V = 234.56
Chi² (χ^2)	1.33	1.74
R_{Bragg}	2.05	2.61

NBT_A

	X	y	z
Na/Bi	0.0000	0.2500	0.0000
Ti	0.254(8)	0.25(3)	0.735(10)
O1	0.01(2)	0.295(14)	0.47(3)
O2	0.252(18)	0.512(17)	−0.07(3)
O3	0.232(17)	0.037(13)	−0.05(3)

NBT_R

	X	y	z
Na/Bi	0.0000	0.2500	0.0000
Ti	0.257(4)	0.255(19)	0.726(7)
O1	0.026(11)	0.188(14)	0.454(16)
O2	0.234(16)	0.510(17)	−0.088(18)
O3	0.25(2)	0.01(2)	−0.03(2)

C. Goutham, K.V. Ashok Kumar, S.S. Kumar Raavi et al.

difficult to see the structural distortions in perovskite structured NBT. The consideration of monoclinic (Cc) distortion in the NBT system is well documented in the literature [37,38]. Based on the goodness of fit parameter (χ^2) and R_p values, NBT stabilizes in the monoclinic structure was confirmed. Moreover, it was observed that the volume of the NBT_A is less compared to NBT_R ceramics. A complete list of the crystal structure parameters of the NBT ceramics is given in Table 1.

3.2. Grain size distribution and composition analysis

The influence of TiO_2 precursor on the size of cubic morphology NBT powders was investigated via scanning electron microscopy (SEM). The as-synthesized SEM images of NBT_A and NBT_R ceramics prepared using the hydrothermal technique are shown in the supplementary information file. The surface microstructure using FESEM of the thermally sintered samples of NBT_A and NBT_R is shown in Fig. 4. The NBT_R shows a loosely packed uneven distribution of grains with a grain size of ~1.34 ± 0.08 µm, while the NBT_A sample shows a tightly packed even distribution of grains with a grain size of ~7.73 ± 0.56 µm. Some pores which are isolated can be observed in between the grains in the microstructure of the NBT_R sample represented by circles, while a microstructure with closely packed grains and precisely defined boundaries of grains is observed in coarse-grained NBT_A. The distribution of grain size is shown in the inset of their respective SEM images. For attaining better ferroelectric properties, ceramics with larger grain sizes and higher density are preferable [13]. The apparent bulk density measured according to the Archimedes principle is 5.92 g/cm^3 and 5.44 g/cm^3 for NBT_A and NBT_R, respectively.

To determine the composition, EDS mapping and the corresponding elemental distribution pattern were carried out and shown in Fig. 5(a) and (b). The proof of the metal components Na, Bi, and Ti can be seen in the EDS image. The atomic percentage of sodium and bismuth elements thus obtained comes close to the stoichiometric ratios and is roughly calculated to be in an acceptable range of 1:1(±0.2). In addition, the elemental mapping corresponding to elements Na, Bi, Ti, and O depicts the homogeneous distribution over the entire microstructure of NBT_A. An elemental mapping area scan is provided in the supplementary information file.

3.3. Evolution of relaxor nature and evidence of thermal hysteresis

The temperature-dependent relative permittivity for NBT_A and NBT_R samples is measured in the frequency range from 5 to 1000 kHz as shown in Fig. 6 (a) and (b). A comparison of the figures shows a broad permittivity with a lower maximum value in the NBT_R sample as well as a high Curie temperature. The effect of the size of grains in contributing to these changes is analyzed in this section. A parallel plate capacitor model was employed to calculate the real part and imaginary part of the dielectric permittivity ($\varepsilon = \varepsilon' + i\varepsilon''$) using the conductance and capacitance data:

$$\varepsilon' = Cd/\varepsilon_o D$$
$$\varepsilon'' = Gd/\omega\varepsilon_o D$$

where G = conductance, C = capacitance, D = electrode area, d = thickness of the sample, ε_o is the permittivity of free space, and $\omega = 2\pi f$ in Hz.

The dielectric curve of NBT_R shows a relatively broadened maximum, which is consistent with the universal behavior for fine-grain ceramics [39]. At the dielectric maximum, this transition is rounded without large frequency dispersion, which negates the relaxor properties of the diffuse phase transition. Regarding the phase transitions of ferroelectric-antiferroelectric (FE-AFE) and antiferroelectric-paraelectric (AFE-PE), the two samples show different signatures, as shown by dotted circles in Fig. 6(a)−(b). During the heating and cooling process, two dielectric anomalies were observed for both samples: a shoulder on the side with lower temperature below 200 °C, known as the depolarization temperature (T_d) with strong frequency dispersion, a diffused phase transition peak on the side with higher temperature around 330 °C (T_m) with weak frequency dispersion. The FE-AFE phase transition in NBT_R is clearly visible, while on the other hand a barely perceptible, highly diffuse, and broadened feature is observed in the NBT_A sample. The NBT_A sample showed a maximum permittivity temperature T_m that was slightly higher than the NBT_R sample has shown in Fig. 6 (a). The increase in T_m with reduced size of grains is because of the internal stresses which are developed during cooling after sintering [40,41]. Interestingly, the NBT_R ceramics dielectric curve is broader compared to NBT_A ceramics.

The sudden drop in the dielectric permittivity values in a ferroelectric material after the transition temperature usually follows the *Curie-Weiss* law,

$$\varepsilon' = C/(T - T_{CW})$$

Here, T_{CW} is the *Curie-Weiss* temperature which relates to the transition temperature of the ferroelectric, and C is the *Curie-Weiss* constant. A deviation from *Curie-Weiss* law for temperatures $T > T_m$ was observed by fitting a straight line between $1/\varepsilon'$ and
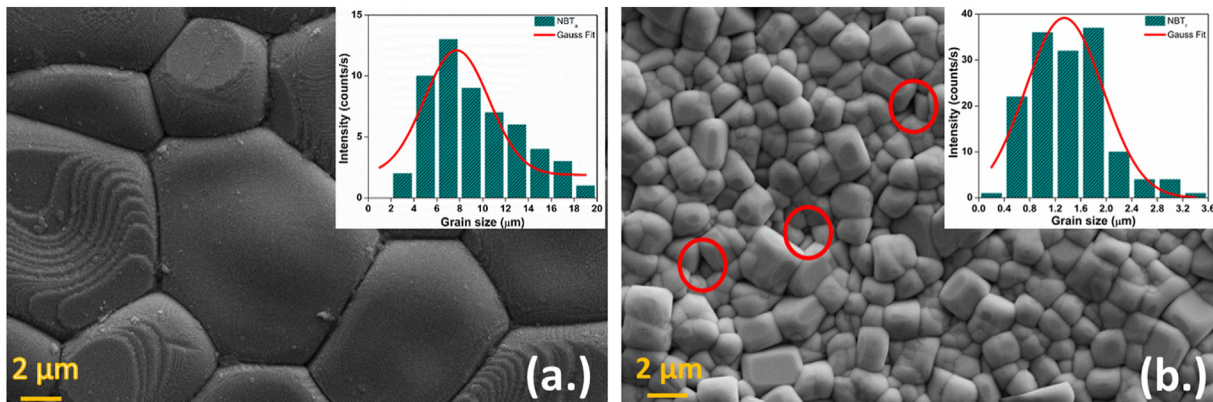

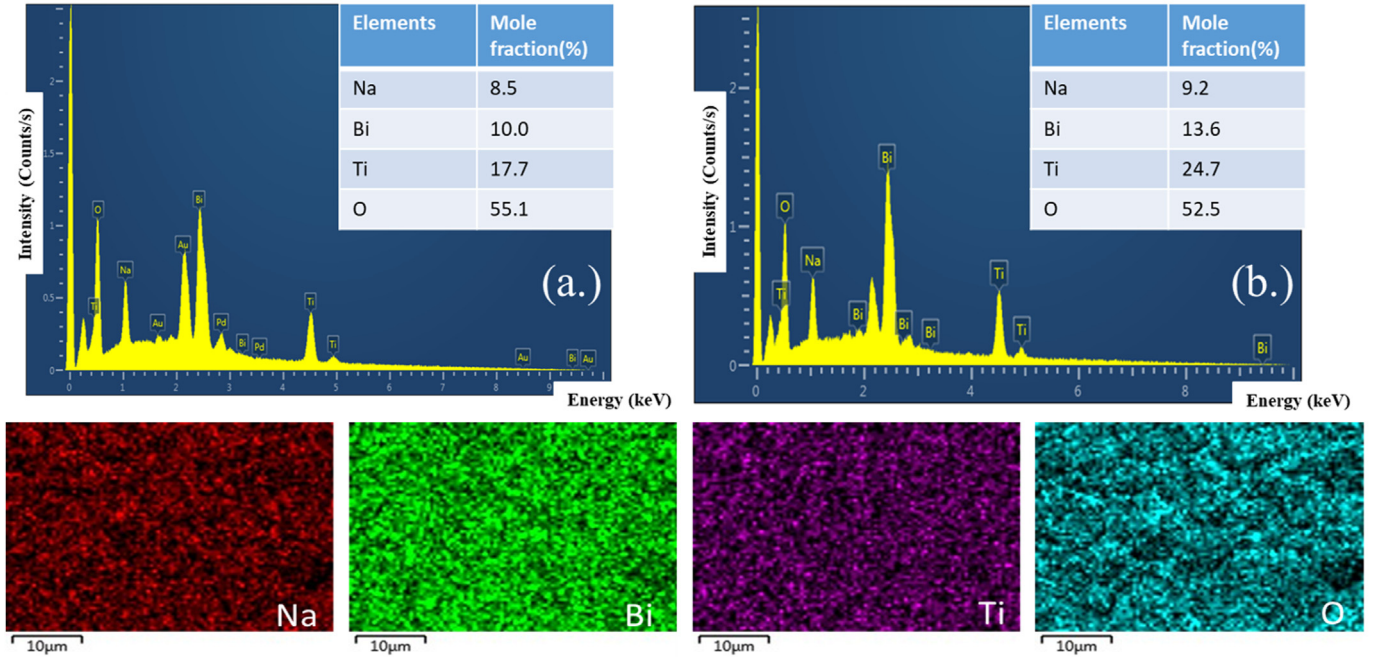**Fig. 4.** Scanning electron micrographs of (a) NBT_A and (b) NBT_R ceramics.

C. Goutham, K.V. Ashok Kumar, S.S. Kumar Raavi et al.

Fig. 5. SEM-EDS of (a) NBT_A and (b) NBT_R samples. Elemental mapping of NBT_A sample.
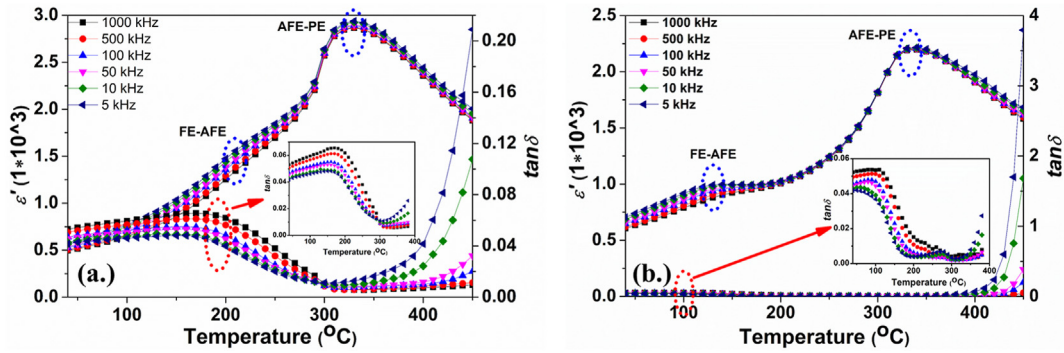

Fig. 6. Comparison of the dielectric constant in (a) NBT_a and (b) NBT_r samples as a function of temperature.

temperature and the T_{CW} was determined from extrapolating the fitted line onto the temperature axis (as shown in Fig. 7(a)−(b)). Burns's temperature (T_B) defines the temperature where $1/_{\varepsilon'}$ starts deviating from the temperature linearly. T_B appears as an indication of the transition between the order-disorder dynamics and the soft-modes in the case of relaxor ferroelectrics.

The dielectric constant (at 100 kHz) above T_m is adjusted further by using the quadratic law to study the properties of the relaxors. The modified *Curie-Weiss* law was used to estimate the degree of diffuseness of the ferroelectric-paraelectric phase transition [42],:

$$\frac{1}{\varepsilon'} - \frac{1}{\varepsilon'_m} = \frac{(T - T_m)^\gamma}{C}$$

where γ is the diffuseness exponent that determines the degree of relative broadness/diffusiveness in the dielectric spectra and ranges from 1 for normal ferroelectrics to 2 for ideal relaxor ferroelectrics, ε'_m is the dielectric constant (maximum) at maximum permittivity temperature (T_m), C is a constant value. The logarithmic curves which are fitted linearly are shown in Fig. 7(c)−(d) with a critical

exponent, where the γ values as obtained from the slope for NBT_A, and NBT_R are 1.58 and 1.75, respectively. This indicates that the NBT_R ceramics are approaching the ideal relaxor nature. The plausible cause for the width or diffusiveness could be due to the large proportion of grain boundaries which causes the internal stresses in the fine grain ceramics, which remains as compressive stress and thus promotes diffuseness. In addition to internal stresses, microscopic heterogeneity in ceramics is caused by structural disturbances and/or compositional fluctuation [39,43,44]. Thus, a higher value of γ in the NBT_R ceramics was explained.

Further, it is noticed that the permittivity in the NBT_R ceramics is significantly reduced compared to NBT_A ceramics (Fig. 6(a)−(b)) which is a well-established implication of grain size refinement [41,43,45−47]. The presence of grain boundaries that are non-ferroelectric with low permittivity is associated with the "dilution effect" and leads to a fall in permittivity values [48,49]. Thus, the grain size decrement increases the proportion of areas with lower permittivity regions. In addition to it, the internal stress distribution on the grains is also increased. This leads to a decrease in the relative permittivity of the ceramics, as noticed in the NBT_R sample.
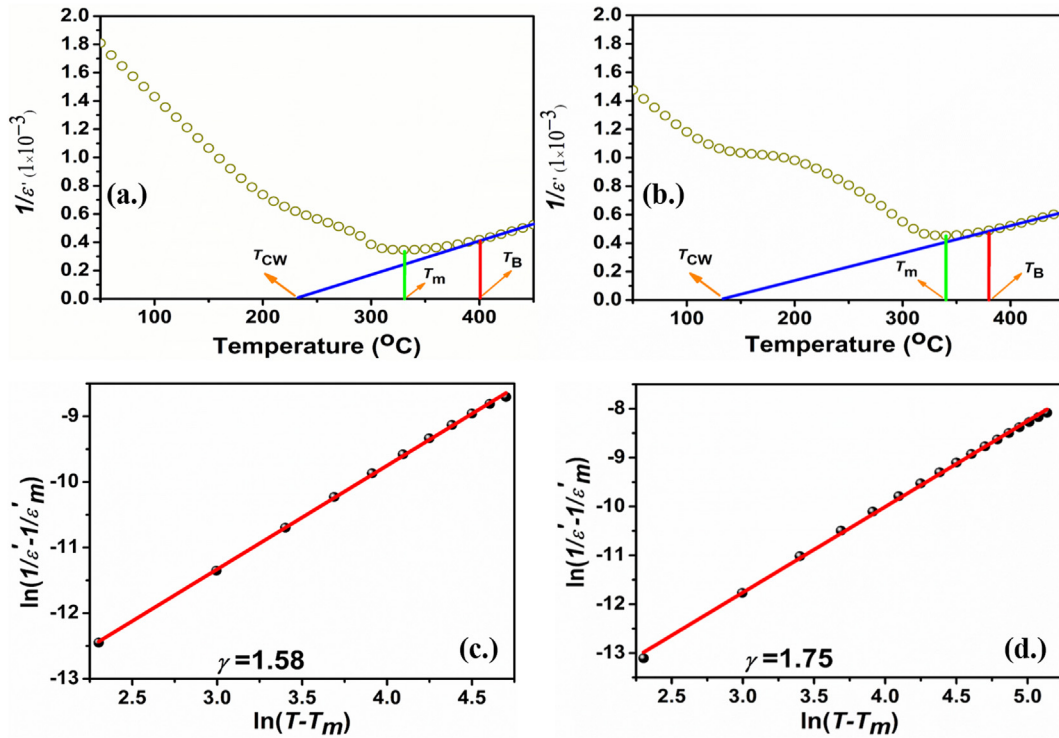
Fig. 7. (a) and 7(b) show the Curie-Weiss law deviation of NBT$_A$ and NBT$_R$ ceramics. 7(c) and 7(d) shows the diffusive parameter of NBT$_A$ and NBT$_R$.

In addition, it is assumed that intrinsic factors such as the unit cell volume and the unit cell distortion parameter have a predominant influence on the temperature of phase transition. The shift in T_m to higher temperatures is a result of the expansion of the unit cell volume as observed in present studies where the fine-grained NBT$_R$ ceramics are more difficult to relieve the stresses due to ferroelectric deformation, which results in grains with few unrelieved stresses [50−52]. Besides, random field effects and cations with multiple valences that occupy equivalent lattice positions are also the origins of an elevated phase transition temperature [53,54].

The dependence of the loss tangent (tanδ) on the temperature for NBT$_A$ and NBT$_R$ samples is shown in Fig. 6(a)−(b) along with its behavior in the lower temperatures which is enlarged in the insets. Anomalies in the loss tangent curve can be seen around the phase transitions: ferroelectric-antiferroelectric (FE-AFE) and antiferroelectric-paraelectric (AFE-PE). A contrasting character was observed in the comparison of loss tangent at various temperature ranges. For the higher temperatures (>400 °C) NBT$_R$ loss tangent is higher whereas in lower temperatures (below T_d), the NBT$_R$ loss tangent is lower and this behavior is because of irreversible domain wall movement [55]. Because of the dissolution of domains above T_m, there is no wall motion contribution in NBT$_A$ as compared to NBT$_R$, which explains the lower value of the loss tangent.

The permittivity curves of NBT ceramics when heated and cooled show a remarkable difference, as shown in Fig. 8(a) and (b). This dielectric thermal hysteresis in the range of 130−340 °C for NBT$_R$ and 270−320 °C for NBT$_A$ indicates a diffuse first-order transition from mixed FE and AFE phases present in the intermediate temperature region to the PE phase, as observed in the single crystals of BNT7BT and Zr-doped BNT7.5BT samples [56]. In addition, NBT material has a complex structure at the A-site sublattices of the perovskite unit cell with irregular occupancy of Bi^{3+} and Na$^+$ ions, thereby forming polar nano regions (PNRs). The chemical disorder in the arrangement of various cations on the analogous lattice sites [57], induces the relaxor nature in the ceramics. This

microscopic property of the relaxor is directly related to PNRs, as demonstrated by Burns and Dacol [58]. The origin of PNRs through the disorder in the cation arrangement is investigated in similar systems like NBT [59], NBT-CT [60], NBT-BT [56], PMN [61]. These nanoregions have different Curie temperatures (T_c) and dielectric behaviors which leads to phase transitions that are diffused. Pu et al. [62] and Zang *et al.* [63] suggested that the transition of phase from LT-PNRs (low-temperature PNRs) to HT-PNRs (high-temperature PNRs) is different while heating and cooling and is the reason for observed dielectric thermal hysteresis. The presence of LT-PNRs at a higher temperature (i.e., higher FE-AFE transition) enfeeble the phase transition contribution from LT-PNRs to HT-PNRs thus leading to a narrowing of the thermal hysteresis loop, as observed in NBT$_A$.

3.4. Role of intergrown orthorhombic phases in suppressing the FE-AFE transition

The first derivative of the relative permittivity ($\delta\varepsilon'/\delta T$) against temperature ($T$) for NBT$_A$ and NBT$_R$ ceramics was plotted in Fig. 8(c) and (d) to find the character of the phase transition involved. Since ε' and the order parameter which is polarization (P) is directly proportional, the sudden accentuation of ε' around T_m is a first-order phase transition signature in both NBT$_A$ and NBT$_R$ ceramics. Further, $\delta\varepsilon'/\delta T$ vs. T(°C) plot depicts a decrease in the anomaly at the corresponding temperature as well as suppression in the proximity of the FE-AFE transition in the NBT$_R$ sample as compared to the NBT$_A$ sample. Electron diffraction studies in the NBT system showed that at around 150−200 °C there is a planar defect corresponding to intergrown orthorhombic *Pnma* layers (a$^-$b$^+$a$^-$) that exist together with the *R3c* (a$^-$a$^-$a$^-$) block matrix which leads to twin planes. The oxygen octahedral strain fluctuation results in the *Pnma* phase formation as shown in Fig. 8(e). With a rise in temperature above 200 °C and reduced *R3c* blocks, more twins appear, as a result of which the polar vectors that are between two consecutive *R3c*

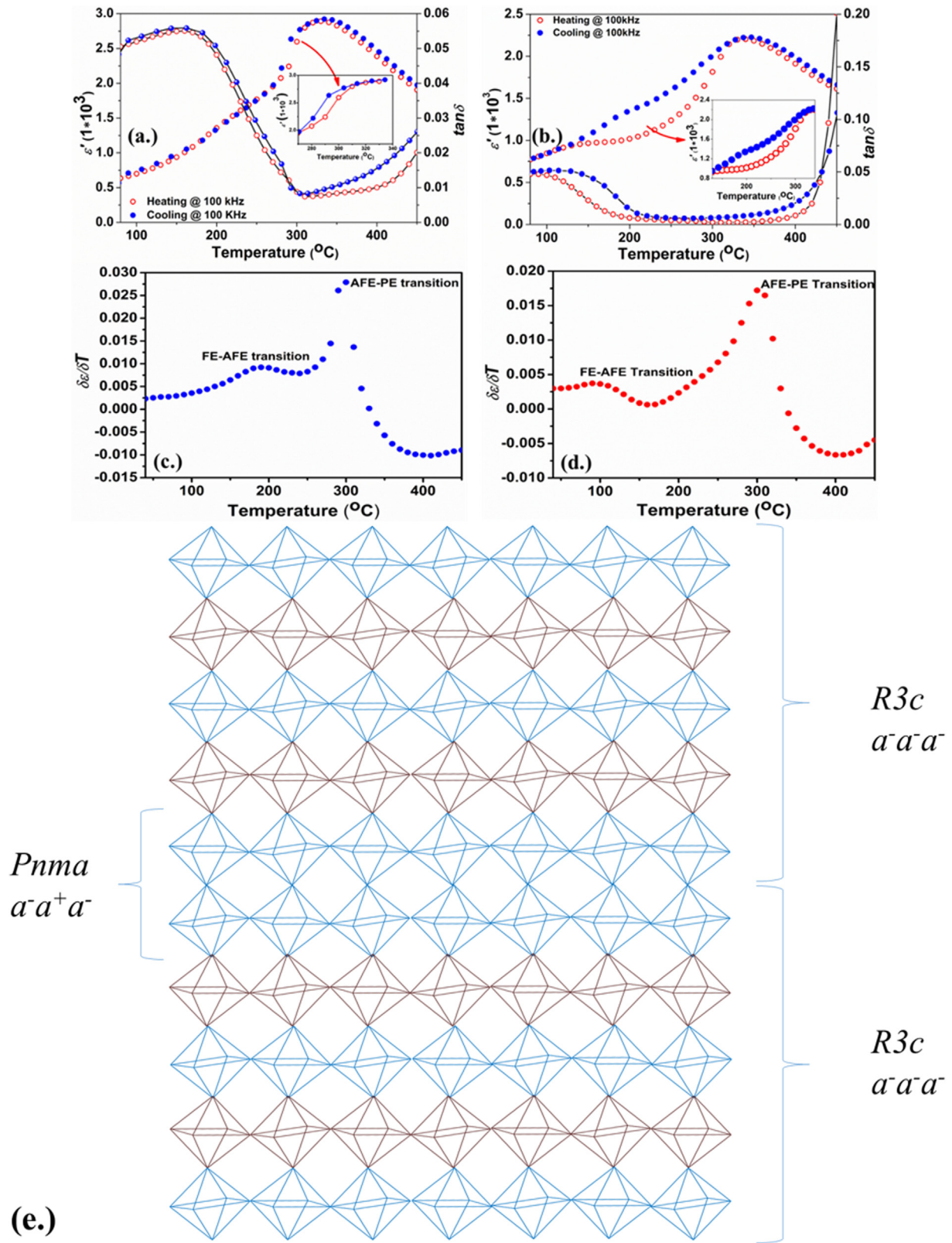C. Goutham, K.V. Ashok Kumar, S.S. Kumar Raavi et al.

Fig. 8. Permittivity curves upon heating and cooling in (a) NBT_A and (b) NBT_R. The variation of $\delta\varepsilon/\delta T$ against temperature (°C) plot for (c) NBT_A and (d) NBT_R samples signifying AFE ordering suppression. (e) Schematic representation of $Pnma$ phase formation between two $R3c$ domains.

blocks are aligned in contrasting directions by a twin plane vertical to the planar direction. This leads to the first abnormality in the dielectric response corresponding to AFE ordering. A jump/anomaly in the derivative graph by 200 °C and 100 °C for NBT_A and NBT_R indicates the FE-AFE transition. Moreover, the AFE-PE transition is distinctly noticeable for both samples at T_m [64].

3.5. Variation of the piezoelectric and ferroelectric parameters

The response due to electromechanical measurements in the polycrystalline ceramics involves many contributions but mainly divided into two categories: (i) the extrinsic contributions, mainly because of the movement of non-180° (ferroelectric-ferroelastic) domain walls, and (ii) the intrinsic contribution, relating the lattice distortion response (inherent and reversible) with respect to external field [55,65,66]. The extrinsic contribution attributes to the dissimilarities in the ferroelectric and piezoelectric properties of coarse- and fine-grained ceramics below the transition temperature. Orihara *et al.* [67] suggested that the proportion of grains that contribute to polarization reversal increases with grain size increment. Although the domain density increment is observed in fine-grained ceramics, the intrinsic response decreases because of the increment in domain walls elastic stiffness as depicted in the schematic microstructure models of coarse (NBT_A)- and fine (NBT_R)-grained ceramics shown in Fig. 9(c) and (d) [68]. In addition, for the moving domains, the boundaries of grains serve as pinning centers. Domain reorientation can be reduced by locking the domain walls at the boundaries of grains, which in turn limits domain wall movement.

Consequently, the higher volume of the grain boundaries and an increase in the elastic stiffness influence the external contribution to the properties. Thus, there is a decrement in the remnant polarization because of the decrease in aligned domains. The polarization-electric field (*P-E*) hysteresis loops, current-electric

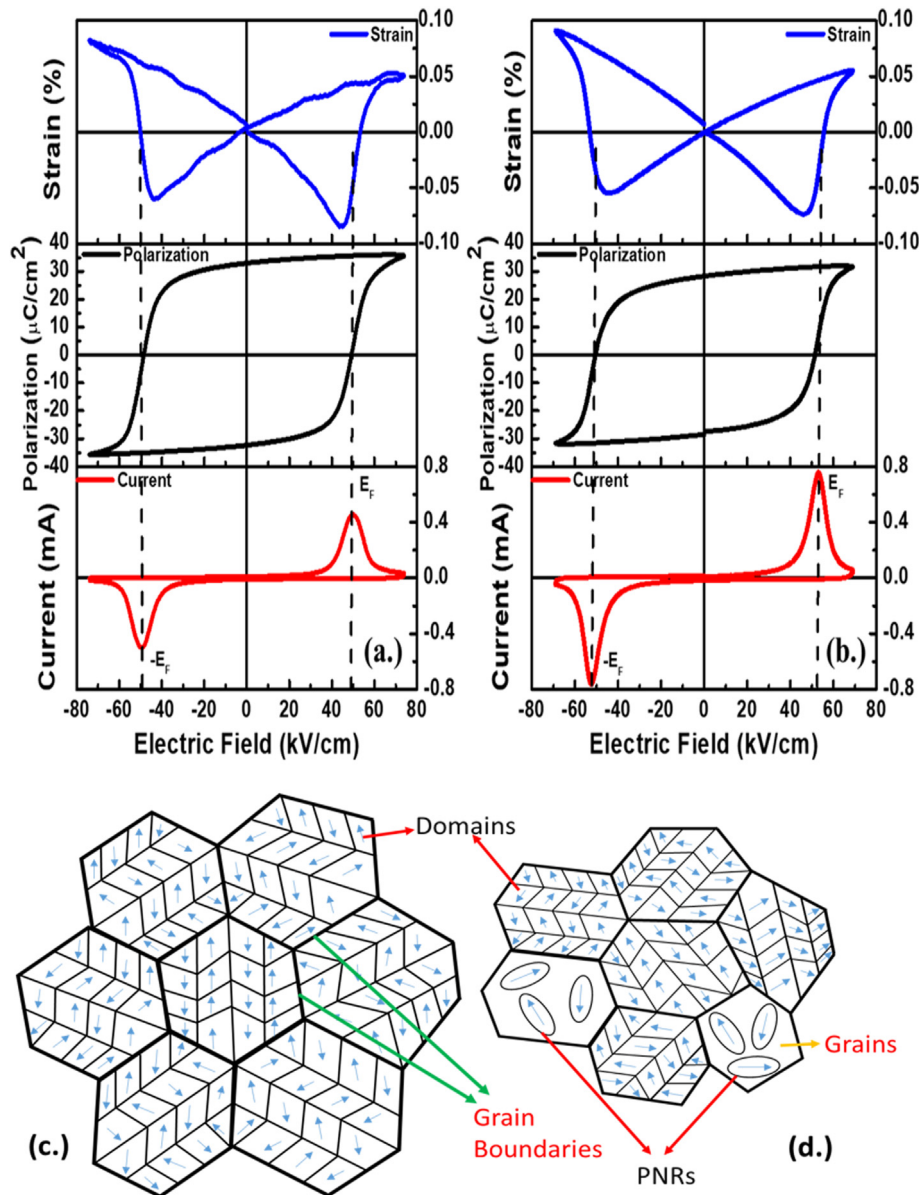**Fig. 9.** Polarization-Electric (*P-E*) field, Current-Electric (*I-E*) field, and Strain-Electric (*S-E*) field loops of (a) NBT_A and (b) NBT_R. The schematic microstructure models of coarse-grained (NBT_A) and fine-grained (NBT_R) ceramics are shown in 9(c) and 9(d) depicting an increment in the domain walls elastic stiffness in NBT_R as compared to NBT_A.

C. Goutham, K.V. Ashok Kumar, S.S. Kumar Raavi et al.

Table 2
The grain size, ferroelectric, and dielectric properties comparison in NBT ceramics prepared through hydrothermal technique as well as conventional solid-state method.

NBT systems	Grain size (μm)	ε' (RT)	ε_m (~ at 100 kHz)	T_m (°C)	γ	P_r (μC/cm^2)	E_c (kV/cm)	T_d (°C)
[70]	–	–	2854	373	–	37.3	59.7	184
[71]	–	638	3500	340	1.29	2.76	12.31	–
[72]	–	–	3132	–	–	23.7	65.2	–
[73]	26.2	633	4000	295.6	–	–	–	201.2
[10]	14	–	3100	320	1.53	38	63	150
[74]	9.49	~350	~2850	~320	1.57	37.45	60	–
[75]	–	–	2573	301	1.58	–	–	–
[76]	–	773	3500	298	–	–	–	–
[77]	–	–	1020	333	1.42	2.55	20	210
[14]	5.6	~650	2700	330	1.67	32.8	56.18	160
[78]	8.5	–	2800	320	–	32.5	68	140
NBT$_A$ (Our Work)	7.73	~500	2900	330	1.58	33.03	49.45	190
NBT$_R$ (Our Work)	1.34	~600	2400	340	1.75	28.34	51.66	110

Reference 10,14, 70−78 are for NBT ceramics prepared through the conventional solid-state method. NBT$_A$ and NBT$_R$ ceramic samples are synthesized using the hydrothermal method.

field (*I-E*) loops, and bipolar strain-electric field (*S-E*) curves of NBT$_A$ and NBT$_R$ are measured at a drive frequency of 1Hz under ambient conditions as shown in Fig. 9, respectively. Domain switching fields observed in *I-E* curves supports that the *P-E* loop of NBT ceramics is almost saturated. In addition, the ferroelectric properties of the ceramics are also greatly affected when the anatase- and rutile-type TiO$_2$ is changed.

Both samples (NBT$_A$ and NBT$_R$) show a P-E loop reminiscent of the ferroelectric materials. However, a slight difference is observed in their shape, coercive fields (E_c), remnant polarization (P_r), and saturated polarization (P_{max}). The P_{max} and P_r values for the NBT$_A$ sample are ~35.71 μC/cm^2 and ~33.03 μC/cm^2 is more as compared to the NBT$_R$ sample i.e. ~31.71 μC/cm^2 and ~28.34 μC/cm^2. The coercive fields, E_c determined from loops for NBT$_A$ is ~49.45 kV/cm and for NBT$_R$ is ~51.66 kV/cm. The remnant polarization (P_r) of the NBT$_A$ ceramics shows a larger value compared to NBT$_R$ samples whereas E_c changes slightly. The E_c increment in NBT$_R$ samples indicates the influence of grain size with a higher volume fraction of grain boundaries on the ferroelectric properties and also in the case of lesser permittivity [69]. E_c is the electric field corresponding to the current peak and coincides with the field at $P = 0$. A typical butterfly-shaped strain loop is seen in NBT$_A$ with a maximum strain of ~0.082%, which is close to the value achieved in the NBT$_R$ sample, which shows a value of ~0.09%. Both samples also show "negative strain" (the strain at zero electric fields subtracted from the lowest strain) of ~0.059% for NBT$_A$ and ~0.055% for NBT$_R$, which is also the normal ferroelectric state by the long-range domain stabilization. In addition, NBT$_A$ ceramics have a uniform grain microstructure, which can also help to improve the electrical properties, as shown above. A comparison of the obtained electrical parameters of NBT$_A$ and NBT$_R$ ceramic samples with NBT prepared through the conventional solid-state method is provided in Table 2.

The bandgap energy (3.2 eV) of anatase-type TiO$_2$ is higher than the rutile-type TiO$_2$ (3 eV) because of which it possesses better reaction activity during the calcination and sintering process of ceramics due to the structural properties of TiO$_2$. In the anatase

structure, the Ti-Ti distances are larger compared to the rutile structure of TiO$_2$, while the distance between Ti-O is shorter. These lead to different electronic configurations and changes in mass density. During the calcination process, there is a significant TiO$_2$ phase change that is resulting in the covalent energy change between the O-Ti-O bonds, which further influences the phase structure of the ceramics and leads to improved electrical performances [16,79]. These results suggest that the NBT compounds synthesized via TiO$_2$ anatase as a precursor are better suited for switchable applications such as ferroelectric tunnel junction, ferroelectric random access memory, etc. as compared to ceramics prepared using TiO$_2$ rutile precursor.

3.6. Effect of structural phases on photocatalytic activities

Ferroelectric materials effectively separate photo-generated carriers (electrons and holes) because of the crystal lattice asymmetry associated electric field (internal) which creates a space charge layer in these materials similar to that in a p-n junction. Therefore, the dye molecules absorbed on the catalyst surfaces are the most important step and lead to the decolorization process. Before unilluminating to the solar radiation, the catalyst dye solutions were stirred for 30 min to attain adsorption-desorption equilibrium between catalyst and dye solution in the dark environment. UV−Visible absorption spectrometer was used to determine the quantity of dye absorbed by the catalyst in the dark condition. To take advantage of the photocatalytic property of NBT, a time-dependent degradation of various dyes was observed. When irradiated with visible light from simulated visible light (400−700 nm), photocatalytic excitons (electrons and holes) are generated by the excitation of NBT catalysts. The water molecules react with holes that are present at the valence band and produce hydroxyl radicals ($OH^•$). The electrons present at the conduction band will react with atmospheric/dissolved oxygen to form $O_2^{-•}$. $O_2^{-•}$ reacts with water and creates $OH^•$, which further reacts with dyes specified to be converted into non-toxic products such as H$_2$O

Table 3
Rate constants of NBT$_A$ and NBT$_R$ catalysts with various dyes.

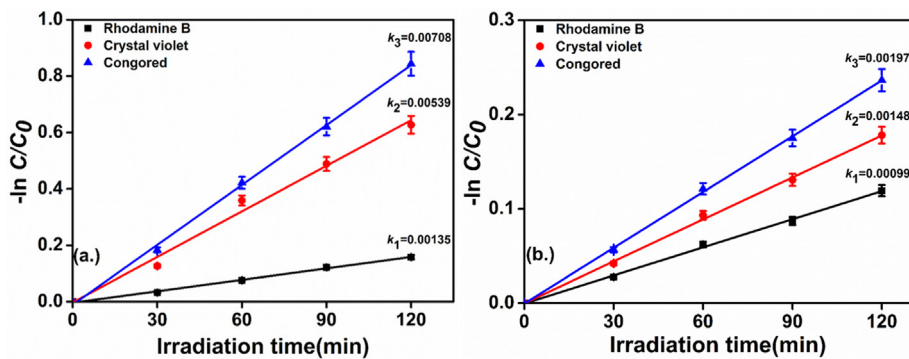| Dye degraded	Dye solution concentration and volume	Catalyst	k_{obs} (min^{-1})
Congo red	100 mg/L, 50 mL	NBT$_A$, 50 mg	0.0071
Congo red	100 mg/L, 50 mL	NBT$_R$, 50 mg	0.0020
Crystal Violet	100 mg/L, 50 mL	NBT$_A$, 50 mg	0.0054
Crystal Violet	100 mg/L, 50 mL	NBT$_R$, 50 mg	0.0015
Rhodamine B	100 mg/L, 50 mL	NBT$_A$, 50 mg	0.0014
Rhodamine B	100 mg/L, 50 mL	NBT$_R$, 50 mg	0.0010

Fig. 10. First-order kinetics plots of (a) NBT$_A$ and (b) NBT$_R$; exposure time-120 min, amount of catalyst -50 mgL^{-1}, the concentration of dye - 50 ppm (The error bars indicate standard deviation).

and CO$_2$ [27,80,81].

Kinetics of the photocatalytic decolorization of various organic dyes with the NBT catalyst follows the Langmuir-Hinshelwood model:

$$r_i = -\frac{dC_i}{dt} = \frac{\kappa K C_i}{1 + \kappa K C_i}$$

where C_i is the dye solution's molar concentration, κ is the rate constant of the reaction, and K is the dye adsorption coefficient on the catalyst. If C_i is small ($C_i < 10^{-3}$ mol/L)^3 and $\kappa K C_i \ll 1$ then the above equation is reduced to a pseudo-first-order kinetics reaction, and the corresponding rate equation is shown below [82−84]:

$$r_i = -\frac{dC_i}{dt} = \kappa K C_i$$

Integrating the above equation gives

$$\ln\left(\frac{C_o}{C}\right) = \kappa_{obs} t$$

where C_o and C are representing the initial and final dye concentration and $\kappa_{obs} = \kappa K$ is the rate constant (observed) of the pseudo-first-order reaction. Therefore, the rate constant data, k_{obs} is calculated from the slope of $\ln(C/C_o)$ vs t and shown in Table 3. The dye solution concentration (C) is determined using Beer-Lambert's law-based spectrophotometer through the absorption measurement value λ_{max}, in which the concentration and the absorbance are directly proportional.

Fig. 10 represents the kinetic plots for photocatalysts NBT$_A$ and NBT$_R$ ceramics and photocatalytic activity of these catalysts are tested by removal of three dyes (Congo red, Crystal violet, and Rhodamine B) with a concentration of 50 mg/L and 50 mg catalyst amount. The photocatalytic degradation of dyes follows pseudo first-order kinetics and it has been observed that the rate constant for the NBT$_A$ catalyst is higher compared to the NBT$_R$ catalyst, and the NBT$_A$ catalyst has shown a higher rate constant value for Congo red dye compared to remaining dyes. The particle size and specific surface area play a key role in the photocatalytic degradation process. A photocatalyst with a high specific surface area and smaller particle size shows the highest activity and higher degradation percentages under visible light irradiation. N$_2$ adsorption/desorption isotherms of NBT$_A$ and NBT$_R$ photocatalysts are shown in the supplementary information file. The surface area measured using a BET analyzer for NBT$_A$ and NBT$_R$ samples is found to be 6.5 m^2/g and 3 m^2/g, respectively. The NBT$_A$ catalyst has a high specific surface area and smaller particle size (225 nm) compared to the NBT$_R$ catalyst. Due to the high specific surface area of NBT$_A$ catalyst, it

provides more surface sites for the degradation process and shows higher photocatalytic activity for degradation of dyes in the aqueous solution. The reactive species involved in the degradation process are determined by scavenger experiments and detailed discussion was displayed in the supplementary information file. Thus, NBT$_A$ is one of the feasible candidates as a piezo-photo catalyst that represents multi-functionality in terms of photo-catalysis along with piezoelectric properties.

4. Conclusions

In summary, it can be said that lead-free piezoelectric NBT ceramics, which were synthesized using the hydrothermal technique with different phase structures of TiO$_2$ (TiO$_2$ anatase and TiO$_2$ rutile) as raw materials, have significantly dissimilar microstructural and electrical properties. NBT samples prepared using TiO$_2$ anatase shows better physical properties like average grain size of ~7.73 μm with coarse grains, higher density and dielectric constant, and larger remnant polarization juxtaposed to NBT samples prepared using TiO$_2$ rutile precursor with an average grain size of ~1.34 μm. Moreover, the differences in grain size of NBT$_A$ and NBT$_R$ samples resulted in the variation of electrical properties. It is assumed that lower dielectric maximum and diffusiveness increment in the NBT$_R$ sample is due to the grain size decrement and the grain boundary density increment as compared to the NBT$_A$ sample. NBT$_R$ also exhibits reduced ferroelectric properties, which is due to the increased internal stress from the reduced domain wall movements because of the larger grain boundaries volume fraction surrounding the grains. The effect of the selection of the precursor on the electrical properties of NBT samples can be illustrated from the above results and determines the application of these materials in various sophisticated devices.

Declaration of competing interest

The authors declare that they have no known competing financial interests or personal relationships that could have appeared to influence the work reported in this paper.

C. Goutham, K.V. Ashok Kumar, S.S. Kumar Raavi et al.

Journal of Materiomics xxx (xxxx) xxx

References

[1] Sczancoski J, Cavalcante L, Badapanda T, Rout S, Panigrahi S, Mastelaro VR, Varela JA, Li MS, Longo E. Solid State Sci 2010;12(7):1160–7.
[2] Jaffe B. Elsevier 2012.
[3] Zhang S, Li F, Jiang X, Kim J, Luo J, Geng X. Prog Mater Sci 2015;68:1–66.
[4] Chen J, Li Q, Jin G, Cheng J. Joint IEEE international symposium on the applications of ferroelectric (ISAF), international symposium on integrated functionalities (ISIF), and piezoelectric force microscopy workshop (PFM). IEEE; 2015. p. 284–7. 2015.
[5] Coondoo I, Panwar N, Kholkin A. J. Adv. Dielectrics 2013:1330002. https://doi.org/10.1142/s2010135x13300028. 03(02).
[6] Liao Y, Xiao D, Lin D. Appl Phys A 2008;90(1):165–9.
[7] Panda P. J Mater Sci 2009;44(19):5049–62.
[8] Guo Y, Kakimoto K-i, Ohsato H. Appl Phys Lett 2004;85(18):4121–3.
[9] Takenaka T, Sakata K. Ferroelectrics 1989;95(1):153–6.
[10] Niranjan MK, Karthik T, Asthana S, Pan J, Waghmare UV. J Appl Phys 2013;113(19):194106.
[11] Karthik T, Radhakrishanan D, Narayana C, Asthana S. J Alloys Compd 2018;732:945–51.
[12] Sahu M, Karthik T, Srinivas A, Asthana S. J Mater Sci Mater Electron 2015;26(12):9741–6.
[13] Tan Y, Zhang J, Wu Y, Wang C, Koval V, Shi B, Ye H, McKinnon R, Viola G, Yan H. Sci Rep 2015;5:9953.
[14] Cilaveni G, Kumar KA, Raavi SSK, Subrahmanyam C, Asthana S. J Alloys Compd 2019;798:540–52.
[15] Hanaor DA, Sorrell CC. J Mater Sci 2011;46(4):855–74.
[16] Chiang C-S, Lee Y-C, Shiao F-T, Lee W-H, Hennings D. J Eur Ceram Soc 2012;32(4):865–73.
[17] Zhou X, Jiang C, Chen C, Luo H, Zhou K, Zhang D. CrystEngComm 2016;18(8):1302–10.
[18] Jing X, Li Y, Yin Q. Mater Sci Eng, B 2003;99(1–3):506–10.
[19] Ma Y, Cho J, Lee Y, Kim B. Mater Chem Phys 2006;98(1):5–8.
[20] Wang Y, Xu G, Yang L, Ren Z, Wei X, Weng W, Du P, Shen G, Han G. Ceram Int 2009;35(4):1657–9.
[21] Lu T, Dai J, Tian J, Song W, Liu X, Lai L, Chu H, Huang X, Liu X. J Alloys Compd 2010;490(1–2):232–5.
[22] Lu R, Yuan J, Shi H, Li B, Wang W, Wang D, Cao M. CrystEngComm 2013;15(19):3984–91.
[23] Li B, Cao MS, Liu J, Wang DW. J Am Ceram Soc 2016;99(7):2316–26.
[24] Mao Y, Park TJ, Zhang F, Zhou H, Wong SS. Small 2007;3(7):1122–39.
[25] Liu Y, Lu Y, Dai S. J Alloys Compd 2009;484(1–2):801–5.
[26] Rauf M, Ashraf SS. J Hazard Mater 2009;166(1):6–16.
[27] Chan SHS, Yeong Wu T, Juan JC, Teh CY. J Chem Tech Biotechnol 2011;86(9):1130–58.
[28] Robinson T, McMullan G, Marchant R, Nigam P. Bioresour Technol 2001;77(3):247–55.
[29] Hoffmann MR, Martin ST, Choi W, Bahnemann DW. Chem Rev 1995;95(1):69–96.
[30] Mills A, Le Hunte S. J Photochem Photobiol Chem 1997;108(1):1–35.
[31] Lee WW, Chung W-H, Huang W-S, Lin W-C, Lin W-Y, Jiang Y-R, Chen C-C. J. Taiwan Inst. Chem. Eng. 2013;44(4):660–9.
[32] Pena M, Fierro J. Chem Rev 2001;101(7):1981–2018.
[33] Seiyama T, Yamazoe N, Eguchi K. Ind Eng Chem Prod Res Dev 1985;24(1):19–27.
[34] Rodriguez-Carvajal J. Laboratoire léon brillouin (CEA-CNRS) version 3. 1990.
[35] Rafiq MA, Costa ME, Vilarinho PM. ACS Appl Mater Interfaces 2016;8(49):33755–64. https://doi.org/10.1021/acsami.6b08199.
[36] Momma K, Izumi F. J Appl Crystallogr 2011;44(6):1272–6.
[37] Aksel E, Forrester JS, Jones JL, Thomas PA, Page K, Suchomel MR. Appl Phys Lett 2011;98(15):152901.
[38] Rao BN, Ranjan R. Phys Rev B 2012;86(13):134103.
[39] Hennings D, Schnell A, Simon G. J Am Ceram Soc 1982;65(11):539–44. https://doi.org/10.1111/j.1151-2916.1982.tb10778.x.
[40] Martirena H, Burfoot J. J Phys C Solid State Phys 1974;7(17):3182.
[41] Randall CA, Kim N, Kucera JP, Cao W, Shrout TR. J Am Ceram Soc 1998;81(3):677–88.
[42] Uchino K, Nomura S. Ferroelectrics 1982;44(1):55–61. https://doi.org/10.1080/00150198208260644.
[43] Tang X-G, Chan HL-W. J Appl Phys 2005;97(3):034109.
[44] Tian Y, Chao X, Wei L, Liang P, Yang Z. J Appl Phys 2013;113(18):184107.
[45] Hao J, Bai W, Li W, Zhai J. J Am Ceram Soc 2012;95(6):1998–2006.
[46] Amorín H, Jiménez R, Deluca M, Ricote J, Hungría T, Castro A, Algueró M. J Am Ceram Soc 2014;97(9):2802–9.
[47] Tan Q, Viehland D. Ferroelectrics 1997;193(1):157–65.
[48] Zhao Z, Buscaglia V, Viviani M, Buscaglia MT, Mitoseriu L, Testino A, Nygren M, Johnsson M, Nanni P. Phys Rev B 2004;70(2):024107.
[49] Polotai AV, Ragulya AV, Randall CA. Ferroelectrics 2003;288(1):93–102.
[50] Zhang L, Zhong W, Wang Y, Zhang P. Solid State Commun 1997;104(5):263–6.
[51] Merz WJ. Phys Rev 1950;78(1):52.
[52] Samara G. Phys Rev 1966;151(2):378.
[53] Randall CA, Eitel R, Jones B, Shrout TR, Woodward D, Reaney I. J Appl Phys 2004;95(7):3633–9.
[54] Eitel R, Zhang S, Shrout TR, Randall CA, Levin I. J Appl Phys 2004;96(5):2828–31.
[55] Herbiet R, Robels U, Dederichs H, Arlt G. Ferroelectrics 1989;98(1):107–21.
[56] Chen C-S, Chen P-Y, Tu C-S. J Appl Phys 2014;115(1):014105.
[57] Bokov AA, Rodriguez BJ, Zhao X, Ko J-H, Jesse S, Long X, Qu W, Kim TH, Budai JD, Morozovska AN. Zeitschrift fuer Kristallographie 2010;226(2):99.
[58] Burns G, Dacol F. Solid State Commun 1983;48(10):853–6.
[59] Liu L, Ma X, Knapp M, Ehrenberg H, Peng B, Fang L, Hinterstein M. EPL (Europhysics Letters) 2017;118(4):47001.
[60] Roukos R, Zaiter N, Chaumont D. J. Adv. Ceram. 2018;7(2):124–42.
[61] Polinger V, Bersuker IB. Phys Rev B 2018;98(21):214102.
[62] Pu Y, Yao M, Liu H, Frömling T. J Eur Ceram Soc 2016;36(10):2461–8.
[63] Zang J, Jo W, Zhang H, Rödel J. J Eur Ceram Soc 2014;34(1):37–43.
[64] Martirena HT, Burfoot JC. J Phys C Solid State Phys 1974;7(17):3182–92. https://doi.org/10.1088/0022-3719/7/17/024.
[65] Zhang Q, Wang H, Kim N, Cross L. J Appl Phys 1994;75(1):454–9.
[66] Bondarenko EI, Topolov VY, Turik AV. Ferroelectrics Lett 1991;13(1):13–9. https://doi.org/10.1080/07315179108203316.
[67] Orihara H, Hashimoto S, Ishibashi Y. J Phys Soc Jpn 1994;63(3):1031–5. https://doi.org/10.1143/JPSJ.63.1031.
[68] Arlt G, Pertsev N. J Appl Phys 1991;70(4):2283–9.
[69] Nanoscale Ferroelectrics and Multiferroics 2016:512–53. https://doi.org/10.1002/9781118935743.ch16.
[70] Guo Y, Fan H, Long S, Shi J, Yang L, Lei S. J Alloys Compd 2014;610:189–95.
[71] Kakroo S, Kumar A, Mishra S, Singh V, Singh PK. Phase Transitions 2016;89(3):211–20.
[72] Ruth DJ, Sundarakannan B. J Mater Sci Mater Electron 2017;28(21):15907–14.
[73] Kornpom C, Udeye T, Bongkarn T. Integrated Ferroelectrics Int J 2017;177(1):59–68.
[74] Banerjee K, Alvi SB, Rengan AK, Asthana S. J Am Ceram Soc 2019;102(11):6802–16.
[75] Barick B, Choudhary R, Pradhan D. Ceram Int 2013;39(5):5695–704.
[76] Petnoi N, Bomlai P, Jiansirisomboon S, Watcharapasorn A. Ceram Int 2013;39:S113–7.
[77] Parija B, Badapanda T, Rout S, Cavalcante L, Panigrahi S, Longo E, Batista N, Sinha T. Ceram Int 2013;39(5):4877–86.
[78] Kandula KR, Raavi SSK, Asthana S. Ferroelectrics 2017;518(1):23–30.
[79] Hanaor DAH, Sorrell CC. J Mater Sci 2011;46(4):855–74. https://doi.org/10.1007/s10853-010-5113-0.
[80] Mani AD, Raju BR, Xanthopoulos N, Ghosal P, Sreedhar B, Subrahmanyam C. Chem Eng J 2013;228:545–53.
[81] Kumar KA, Chandana L, Ghosal P, Subrahmanyam C. Mol. Catal. 2018;451:87–95.
[82] Konstantinou IK, Albanis TA. Appl Catal B Environ 2004;49(1):1–14.
[83] Herrmann J-M. Catal Today 1999;53(1):115–29.
[84] Baran W, Adamek E, Makowski A. Chem Eng J 2008;145(2):242–8.

Mr. Cilaveni Goutham received his M.Sc. in Physics degree from University of Hyderabad, Hyderabad, India. Currently, he works as a Research Scholar at the Department of Physics, Indian Institute of Technology Hyderabad, Hyderabad, India. His research areas include ceramic processing and characterizations of lead-free ferroelectric materials and enhancing the piezoelectric and dielectric properties of ceramic materials for energy storage and harvesting applications under the supervision of Prof. Saket Asthana.

Dr. Saket Asthana is currently a Professor and Group head of Advanced Functional Materials Laboratory at the Department of Physics, Indian Institute of Technology Hyderabad. His main research focus is on the functional materials to exploit their inherent properties and functions to achieve an intelligent action. He received his M.Tech. in Materials Science and Technology in 2001 with a Gold Medal from IIT BHU and Ph.D degree from IIT Bombay in 2006. He worked as Postdoctoral Researcher as Brain Korea-21 fellow in S Korea, as CEFIPRA and CNRS researcher in France from 2006 to 2010. He is awarded with the JNCASR-visiting fellowship in 2017, DST-Young Scientist Award in 2012 and as Invited Guest Professor at Osaka university in 2011. He has authored around 110 publications and graduated 5 students for Ph.D.